Technique for magnetic moment reconstruction of laser-cooled atoms using direct imaging and prospects for measuring magnetic sublevel distributions

G. Carlse,[1,2] ⓘ A. Pouliot,[1] T. Vacheresse,[1] A. Carew,[1] H. C. Beica,[1] S. Winter,[1] AND A. Kumarakrishnan[1,3]

[1]Department of Physics and Astronomy, York University, 4700 Keele Street, Toronto, Ontario M3J 1P3, Canada
[2]e-mail: gehrig.carlse@gmail.com
[3]e-mail: akumar@yorku.ca

We describe a simple time-of-flight technique for measuring the magnetic moment of an optically pumped magneto-optical trap. The technique relies on free-expansion imaging of a cold atom cloud in a small magnetic field gradient without the need to detect spatial separation between magnetic sublevels. We find that the effective acceleration of the cloud can be used to characterize extreme state optical pumping. In the general case, we show that the integrated displacement of the falling cloud can be accurately modeled using rate equation simulations of magnetic sublevel populations, and knowledge of local magnetic fields, field gradients, and light intensities. The agreement between the model and the data allows the reconstruction of magnetic moments and suggests that this technique may be suitable for the measurement of population distributions over a range of optical pumping conditions.   © 2020 Optical Society of America

https://doi.org/10.1364/JOSAB.388995

1. INTRODUCTION

The realization of magneto-optical traps (MOTs) [1,2] has led to several fascinating experiments relating to many-body interactions that include Feshbach resonances [3], Bose–Einstein condensation (BEC) [4,5], and investigations of Mott insulator transitions [6]. MOTs have also provided reliable samples of cold atoms necessary for atomic frequency standards [7,8] and precision measurements using atom interferometry [9–11]. More recently, MOTs have been developed as portable sensors for remote sensing applications, such as measurements of gravitational acceleration, gravity gradients, and rotations. World-wide efforts to generate MOT-based sensors include aircraft-based freefall experiments [12], cold atom payloads in near-Earth orbits [13], and experiments based on freely falling [14] or rocket-launched BECs [15]. Such experiments rely on magnetic state preparation through optical pumping and efficient methods of characterizing MOTs [16,17]. Therefore, reliable techniques to measure magnetic sublevel distributions are of considerable practical consequence.

While sensitive *in situ* techniques, such as Faraday spectroscopy [18–20] and nonlinear magneto-optical resonance [20,21] have been developed for characterizing magnetic fields,

magnetic field gradients, and monitoring the initial conditions of atom traps, making direct measurements of the magnetic moment and magnetic sublevel populations in a MOT remains a challenging problem. This is primarily because the laser beam configurations involve complex light polarizations that result in optical pumping of a multilevel atom and produce spatially varying population distributions across the sample. A common technique for determining the magnetic sublevel populations is to apply a Zeeman shifting magnetic field after the turn-off of the confining forces, followed by absorption or fluorescence spectroscopy using optical [16,22,23] or RF fields [24,25]. However, such an experiment requires separate probe lasers or RF sources that must be pulsed and scanned across the atomic resonances.

An alternate approach involves dropping state-prepared atoms through a region with a well-defined magnetic field gradient that is sufficiently strong to spatially separate magnetic sublevels, and observing the resulting time-of-flight fluorescence spectra of atoms falling through a sheet of light placed below the cloud. This technique, originally used to characterize population transfer to a target state using adiabatic rapid passage [26], has since been coined the longitudinal Stern–Gerlach

time-of-flight method and has been used to measure magnetic sublevel population distributions in MOTs [27].

In Ref. [27], the atoms fall through a relatively long (∼1 m) zone in which a strong magnetic field gradient is applied resulting in the spatial separation of the individual magnetic sublevel populations along the vertical direction before time-of-flight detection with a sheet of light. The original Stern–Gerlach geometry [28,29] has also been used for measuring population distributions in the atomic beam experiments in Ref. [30]. In Ref. [30], a magnetic field gradient was applied transverse to the direction of the atomic beam so that the magnetic sublevels were physically separated in a downstream imaging plane. The separated states were imaged by applying a perpendicular laser beam and detecting the spatially resolved fluorescence. This type of spatial separation has also been achieved in work involving ultra-cold atoms held in an optical dipole force trap at a temperature < 1 µK [31]. In these experiments, a magnetic field gradient was used to separate and expel all but the $m_f = 0$ sublevels from the trap, where m_f refers to the magnetic quantum number. There is also an entirely separate class of experiments [32–36] that have employed a Stern–Gerlach-like approach for the study of spinor-BECs. As in Ref. [31], the narrow velocity distribution of the sample ensures the center-of-mass separations of different magnetic sublevels, so that their evolution can be imaged.

In this paper, we address a very different problem, namely, the reconstruction of magnetic moments and the possibility of measuring magnetic sublevel populations in relatively hot clouds of atoms, where the velocity distributions of the samples are orders of magnitude larger than those of a BEC. Further, we apply a relatively weak magnetic gradient over a small drop-zone to observe the differential force on the magnetic sublevels. Due to these features, our work also differs from other Stern–Gerlach measurements that use long path lengths [27,30] and much larger magnetic field gradients [26,30] to spatially separate magnetic states. Although spatial separation of the magnetic sublevels is not achieved in our work, we show that free-expansion imaging of the relatively hot, atomic cloud falling in a weak magnetic gradient, combined with trajectory analysis of the center of mass, can serve as an interesting technique for magnetic moment reconstruction [37]. In addition, we show that the integrated cloud displacement provides a convenient metric to quantify the trajectory of the centroid. Our work suggests that it is possible to develop a compact alternative to absorption spectroscopy applicable to relatively hot laser-cooled samples where space constraints preclude the installation of extended time-of-flight setups or drop zones with appreciable magnetic field gradients. Furthermore, our technique is not confined to any particular orientation, since the evolution of the cloud can be accurately tracked and modeled in all three dimensions.

2. OPERATIONAL PRINCIPLES

Free-expansion imaging has proven to be particularly useful for measuring the temperature of cold atomic samples [23,38], while position measurements of the falling cloud allow the gravitational acceleration to be measured with a statistical precision of 0.1% [23]. In the presence of a magnetic gradient

$\partial B_z/\partial z$, atoms in each of the sublevels experience an additional force $F_m = \mu \partial B_z/\partial z$ along the direction of the gradient, where $\mu = \mu_b g_f m_f$ is the magnetic dipole moment. Here, μ_b is the Bohr magneton, and g_f is the Landé g-factor.

We optically pump a cloud of ^{85}Rb atoms to the stretched states of the ground state manifold ($F = 3$, $m_f = \pm 3$) and show that the measured acceleration of the cloud can be used to characterize extreme state optical pumping. For the general case of partial pumping, our work shows that moment reconstruction can be achieved by either fitting to the center-of-mass trajectory or, even more simply, by measuring the integrated displacement of this trajectory to infer the time-dependent evolution of magnetic sublevel populations during optical pumping. Since the dynamics of an optical pumping curve are well understood if the driving fields and polarizations are specified, we rely on such curves to validate the accuracy of our technique. We also find that measurements of the cloud displacement are in good agreement with a model that simulates and integrates cloud displacement. The model relies on magnetic sublevel populations obtained from a multilevel rate equation simulation as well as accurate knowledge of light intensities, magnetic fields, and magnetic field gradients in the vicinity of the falling cloud.

We now describe the experimental setup and diagnostic measurements, followed by the results and discussion of the new technique developed in this paper.

3. EXPERIMENTAL DETAILS

Figure 1(a) shows a schematic diagram of the optical layout for the experiments. The trapping light, derived from an external cavity diode laser (ECDL) [39] is locked 90 MHz below the $F = 3 \rightarrow 4'$ resonance in ^{85}Rb (ω_0) and upshifted with a 235 MHz acousto-optic modulator (AOM). This light seeds a tapered amplifier (TA) with an output power of ∼2 W. The output of the TA, at a frequency of $\omega_0 + 145$ MHz, is dual-passed through a downshifting 80 MHz AOM and directed into two separate optical fibers. The output of one of these fibers produces a horizontal trapping beam oriented along the symmetry axis of the trapping anti-Helmholtz coils, perpendicular to the plane in Fig. 1(b). The output of the second fiber is divided using a fiber splitter to produce two orthogonal beams oriented along the radial direction of the anti-Helmholtz coils, each at 45 deg from the vertical. This configuration produces ∼60 mW in each of the incident trapping beams tuned ∼15 MHz below ω_0. A separate repump laser, locked ∼40 MHz above the $F = 2 \rightarrow 3'$ transition and amplitude modulated by a 40 MHz downshifting AOM, is combined with the trapping light and coupled into fiber #1 and fiber #2.

The non-diffracted beam from the 80 MHz trapping AOM is directed into a third fiber launch. The output of this fiber is frequency downshifted 265 MHz with an AOM to generate an optical pumping beam resonant with the $F = 3 \rightarrow 3'$ transition. A separate ECDL produces a secondary CW repump beam that is combined with the $F = 3 \rightarrow 3'$ optical pumping beam using a 50:50 beam splitter.

The atom trapping vacuum chamber [see Fig. 1(b)] includes a ∼1 m pyrex tube with a square cross section and sides of 10 cm. The outputs of the orthogonal fiber beams are expanded to a diameter of 36 mm and retro-reflected through the center
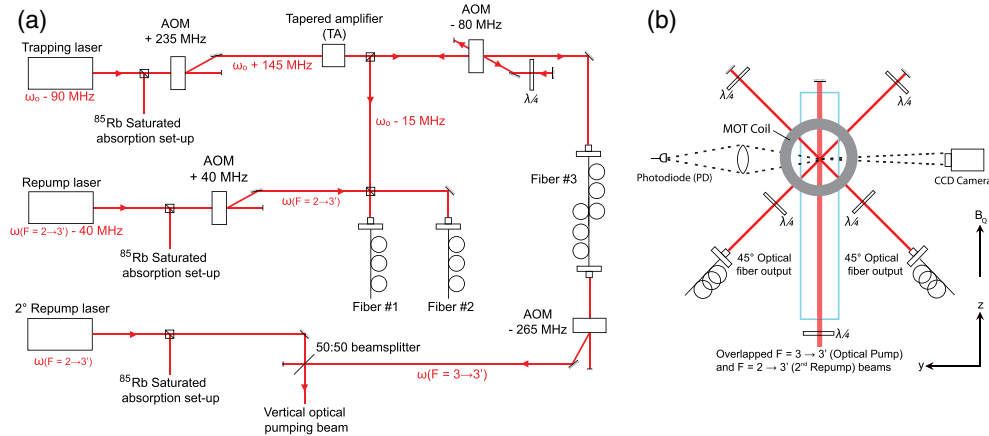
Fig. 1. (a) Schematic diagram of optical layout showing laser frequencies and detunings. The output of fiber #1 produces the horizontal trapping beam, and the output of fiber #2 is split to generate the 45 deg angled trapping beams. (b) Schematic diagram of the trapping vacuum chamber (blue/gray). The horizontal trapping beam travels along the symmetry axis of the anti-Helmholtz MOT coils perpendicular to the plane of the figure. The quantizing magnetic field and the optical pumping beams are aligned along the vertical (z) direction.

of a 40 cm drop zone in the pyrex cell. The magnetic fields and field gradients in the drop zone are suppressed by three pairs of "Helmholtz" and three pairs of "anti-Helmholtz" coils wound on square forms [note that these field and field gradient suppression coils are not shown in Fig. 1(b)]. In previous work, this geometry has proven to be highly suitable for molasses cooling [40–43]. Here, each pair of coils is separated by a distance ~$0.54L$, where L is the side length of the coils and produces uniform fields and field gradients with minimal curvature across the drop zone. Measurements of magnetic fields and field gradients around the drop zone, using a flux-gate magnetometer, suggest passive suppression at levels of ~10 mG and ~1 mG/cm. The longest observation times in these experiments (~60 ms) correspond to cloud displacements of ~2 cm. Over these distances, magnetic field simulations show maximum variations of ~4 mG for magnetic fields and ~2 mG/cm for magnetic field gradients.

Figure 1(b) also shows the trapping anti-Helmholtz coils that have a symmetry axis along the horizontal trapping beam. These coils can be turned off on the time scale of ~200 μs and

turned on in ~10 ms using an integrated gate bi-polar transistor (IGBT). The entire apparatus is vibration isolated using a sub-Hertz platform and a pneumatically supported optical table. Measurements of trap loading (time constant ~20 s) suggest a rubidium vapor pressure of ~10^{-9} Torr inside the pyrex chamber.

Figure 2(a) shows a diagnostic temperature measurement obtained by imaging the free expansion [23]. The images of the cloud in the $x − z$ plane (where x is the horizontal and z is the vertical) are recorded on a CCD camera placed ~55 cm away from the MOT and looking along the y direction, as shown in Fig. 1(b). To acquire each image, the trap is fully loaded with ~2×10^8 atoms. After the turn-off of the magnetic field gradient, and the trapping and repumping beams, the laser beams are turned back on to illuminate the falling cloud after various delay times separated by 1 ms intervals, for up to ~60 ms after cloud release. For each delay interval (or "drop time") 10 individual images are recorded and averaged. During each repetition, the CCD camera shutter is triggered to open for 500 μs, starting at the time at which the trapping and repump beams are turned back on. The data in Fig. 2(a) are fit to a hyperbola given by
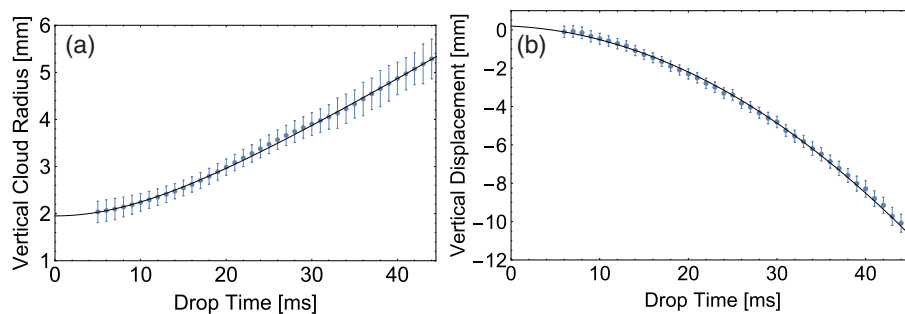

Fig. 2. (a) Ballistic expansion showing the cloud radius as a function of time after cloud release. The fit line of $R(t) = \sqrt{R_0^2 + (ut)^2}$ gives $R_0 = (1.95 \pm 0.01)$ mm, $u = (111.8 \pm 0.4)$ mm/s, and an inferred temperature $T = (63.6 \pm 0.5)$ μK. (b) Centroid displacement of a falling cloud. The fit line of $z(t) = g\,t^2/2 + v_z t + z_0$ gives $z_0 = (0.22 \pm 0.08)$ mm, $v_z = (72.0 \pm 5.1)$ mm/s, and $g = (−9.79 \pm 0.16)$ m/s^2.

$R(t) = \sqrt{R_0^2 + (ut)^2}$, where R_0 is the initial cloud size, and u is the most probable speed of the laser cooled sample. The temperature given by $T = mu^2/(2k_B)$ is ~64 μK.

Figure 2(b) shows the vertical trajectory obtained by tracking the centroid of a falling cloud. To extract the value of gravity, the cloud positions are fit to $z(t) = g t^2/2 + v_z t + z_0$, where g is the gravitational acceleration, v_z is the initial vertical speed due to cloud launch, and z_0 is the initial vertical position. The centroid positions of the clouds are extracted using two-dimensional Gaussian fits to the averaged free-expansion images, and the resulting trajectories are smoothed with a weighted moving average using a Gaussian kernel (2 ms full width), which is small compared to the 50 ms timescale of the entire experiment. The smoothing procedure achieves the same signal-to-noise as a data set that has ~2.5 times more repetitions, and therefore it serves to reduce the data acquisition time. This centroid tracking protocol is utilized throughout this work as the basis for trajectory analysis.

We now explain a different aspect of the experiment, namely, the timing sequence required to optically pump the cloud and change the initial conditions for cloud evolution. Figure 3(a) shows the timing diagram for optically pumping and imaging the falling cloud. After the MOT is fully loaded, the trapping coils are turned off and the atoms are held in a molasses for ~4 ms allowing transient magnetic fields to dissipate. The trapping light is then turned off, followed ~90 μs later by the repump light, to ensure that the $F = 2$ ground state is fully emptied. To study the effects of optical pumping, a vertical quantizing magnetic field of ~200 mG is continuously applied using the large square field cancellation coils. A variable length optical pumping pulse, resonant with the $F = 3 \rightarrow 3'$ transition, is applied ~50 μs after the turn off of the repump beam. As described in Fig. 1, this beam (power ~750 μW) is combined with the secondary repump beam (power ~2.5mW). The two beams are aligned along the vertical and retro-reflected. Both beams have average diameters of ~1.5 cm.

Figure 3(b) shows the fluorescence signal due to optical pumping recorded by a photodetector with a rise time of 400 ns that is ~34 cm from the MOT. If the secondary repump beam is turned off, atoms are optically pumped to the $F = 2$ ground state on a timescale <1 μs as shown by the rapid fluorescence decay. If both optical pumping beams are on and linearly polarized, the fluorescence remains visible for the duration of the

optical pumping pulse. However, if the beams have either σ^+ or σ^- polarization, the atoms are pumped to the stretched states ($F = 3$, $m_f = \pm 3$) on a timescale of ~10 μs. In these σ^+ and σ^- cases, the fluorescence should go to zero when the sample is fully optically pumped because the target states are "dark" to the circularly polarized optical pumping beams. In practice, for this "fully pumped" case, we find a small residual pedestal of fluorescence that we attribute to imperfect polarization of the optical pumping beams.

For the trajectory analysis leading to magnetic state reconstruction, the cloud is imaged as it falls through a time-varying magnetic field gradient arising from re-engaging the trapping coils. This gradient reaches its steady state value in ~10 ms, as noted earlier. Both the transient turn-on and the steady-state value are included in simulations of trajectories. In the timing sequence, the coils are turned on ~100 μs after the optical pumping pulse. In this case, the earliest images are recorded ~9 ms after the turn-on of the coils and ~14 ms after the initial turn-off of the coils [see Fig. 3(a)]. Throughout the paper, we use the steady-state value of the vertical gradient to label the results.

4. RESULTS AND DISCUSSION

A. Effective Acceleration

Figure 4(a) shows the effective acceleration g_{eff} of the falling cloud for three polarizations of the optical pumping beams as a function of the steady-state value of the vertical magnetic field gradient. To avoid sensitivity to the launch velocity, these data are analyzed by tracking the centroid only from the apex point of the trajectories and fitting to the functional form $z(t) = g_{\text{eff}} t^2/2 + z_0$. Here, the optical pumping beam is turned on for 50 μs to ensure the sample is "fully pumped" to the stretched states, as shown in Fig. 3(b). We find that the slopes for σ^+ and σ^- pumping [0.15 ± 0.02 (m/s^2)/(G/cm) and -0.13 ± 0.03 (m/s^2)/(G/cm), respectively] agree within the statistical error and clearly show that extreme state optical pumping can be distinguished with respect to the case of linear pumping for which the slope is zero within experimental error. We also find that the effective acceleration for the linearly pumped case is indistinguishable from the case of no optical pumping. This feature of the data suggests that both in the absence of optical pumping and in the case of linear pumping, the magnetic sublevel populations are symmetrically distributed with respect to the $m_f = 0$ ground state. These inferences
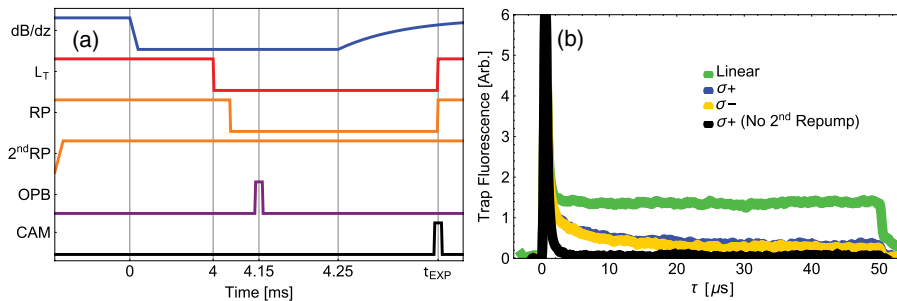

Fig. 3.   (a) Timing diagram showing the turn-on and -off of the magnetic field gradient dB/dz, trapping laser L_T, repump laser RP, secondary repump laser 2$^{\text{nd}}$RP, optical pumping beam OPB, and the camera trigger CAM. The leading edge of the camera trigger t_{EXP}, varies from 14 to 64 ms. (b) Fluorescence imaging for $F = 3 \rightarrow 3'$ optical pumping. Shown as a function of the optical pumping time τ.
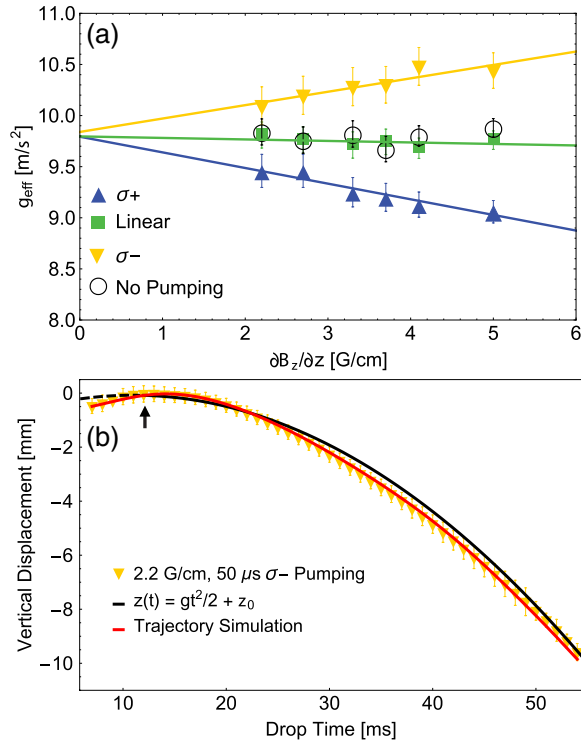
Fig. 4. (a) Effective vertical acceleration of falling clouds as a function of the steady-state magnetic gradient in which they fall. Clouds are optically pumped for 50 μs using σ^+, σ^- and linearly polarized beams. (b) Centroid displacement of a falling cloud in a magnetic field gradient. The fit line (black) gives $z_0 = (-0.08 \pm 0.07)$ mm, and $g = (-10.2 \pm 0.2)$ m/s^2. The apex point, indicated by an arrow, represents the beginning of the fit line. The dashed line starting at the apex points shows the extrapolation of the fit line to earlier times. The red (gray) curve shows a trajectory simulated using Eq. (1a).

---

are supported by rate equation simulations presented later in the paper.

Despite the apparent effectiveness of the parameter g_{eff} as a simple metric to characterize optical pumping, quadratic fits to the trajectory data show noticeable disagreement. To obtain better agreement, we perform comprehensive trajectory analysis that considers the time-varying magnetic fields and magnetic field gradients along the path of the cloud. The resultant trajectories can be contrasted with the case of quadratic fitting using a constant acceleration g_{eff}, as shown in Fig. 4(b).

B. Theoretical Model of Cloud Displacements

It is evident in Fig. 4(b) that the cloud displacement is defined by a time-dependent acceleration due to the differential forces on the magnetic moments in the cloud. Therefore, we model the vertical and horizontal displacements of the falling cloud as functions of drop time t by

$$z(t) = \left(g + \langle \mu(t) \rangle \frac{\partial B_z}{\partial z} \bigg|_{x,y,z,t} \right) \frac{t^2}{2} + v_z t + z_0, \qquad \textbf{(1a)}$$

$$x(t) = \langle \mu(t) \rangle \frac{\partial B_x}{\partial x} \bigg|_{x,y,z,t} \frac{t^2}{2} + v_x t + x_0, \qquad \textbf{(1b)}$$

where $\frac{\partial B_z}{\partial z}\big|_{x,y,z,t}$ and $\frac{\partial B_x}{\partial x}\big|_{x,y,z,t}$ are the magnetic field gradients sampled by the centroid of the cloud and

$$\langle \mu \rangle = \sum_{m_f} \rho_{F,m_f} m_f g_f \mu_b \qquad \textbf{(2)}$$

is the net magnetic moment of the cloud. Here, the ρ_{F,m_f} represents the magnetic sublevel populations. Such a model appears suitable to describe falling clouds in small field gradients over the relatively short drop times in these experiments.

In our case, $\langle \mu(t) \rangle$ is inherently position dependent due to the spatially varying quadrupole magnetic field generated by the trapping coils. The time dependence in $\langle \mu(t) \rangle$ results from the assumption that the magnetic moments of the atoms are able to follow the changing local magnetic field. This requirement is related to the adiabaticity condition for Majorana transitions that project atoms into other magnetic sublevels.

Simulations of these trajectories involve computing the time-dependent magnetic fields and aligning the magnetic moment with the local magnetic field at all times. Such calculations require detailed knowledge of the magnetic fields, field gradients, and laser intensity imbalances (which can produce cloud launch). Good agreement between the model and measurements can allow the reconstruction of the magnetic moments and underlying magnetic sublevel distributions. This can be achieved by matching both the observed vertical and horizontal trajectories with simulations. Figure 4(b) shows a representative vertical trajectory, and Fig. 5(a) shows two horizontal trajectories for opposite pumping conditions. Figure 5(b) shows the spatial profile of an expanding cloud (shaded region) along the horizontal direction as a function of drop time for the σ^+ trajectory shown in Fig. 5(a). The conditions were chosen to correspond to a case of partial pumping to ensure that the population is distributed into multiple magnetic states. The simulated centroid trajectory is superimposed upon this figure, and a fit to the spatial profile for the longest free-expansion time is shown as an inset. This figure illustrates an important aspect of this technique—that it is not necessary to achieve discernible spatial separations between the magnetic sublevels on the timescale of the measurement.

The data in Figs. 4 and 5 also demonstrate the power of free-expansion imaging in tracking the cloud evolution along both the transverse and longitudinal directions due to weak gradients imposed by the same coil. Additionally, we find that the integrated displacements $\int z(t)\,dt$ and $\int x(t)\,dt$, which can be readily calculated, are particularly convenient metrics for comparison between the simulations and experiment.

To facilitate these comparisons with data, we carry out rate equation simulations of the magnetic sublevel populations due to optical pumping, reconstruct the effective magnetic moment of the cloud as a function of the optical pumping time τ, and simulate the trajectory of this moment as it falls through a magnetic field gradient using Eqs. (1a) and (1b).

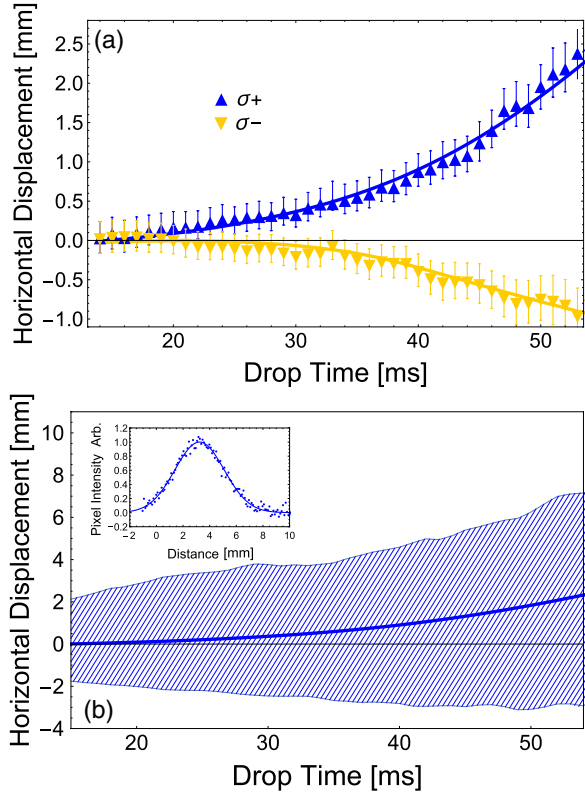These simulations consist of a multilevel rate equation model defined by

Fig. 5. (a) Cloud displacement along the horizontal direction, after partial pumping to extreme states. Each trajectory shows the evolution of a cloud in a vertical magnetic field gradient of 5 G/cm and 1 µs of optical pumping. The solid curves show simulated trajectories for the same magnetic field gradients and optical pumping time for $\sigma+$, blue (dark gray) lines, and $\sigma-$, orange (light gray) lines, polarizations. (b) Horizontal cloud evolution after 1 µs of $\sigma+$ optical pumping in a vertical magnetic field gradient of 5 G/cm. Shaded region shows the cloud profile (i.e., $1/e^2$ diameter). Solid line indicates the simulated centroid position as a function of drop time, and inset shows a Gaussian fit to the horizontal cloud profile after a drop time of 53 ms.

$$\frac{d\rho_{F,m_f}}{d\tau}$$

$$= \sum_{H,m_h} \gamma_{H,F} \begin{pmatrix} H & 1 & F \\ m_h & q & m_f \end{pmatrix}^2 \rho_{H,m_h}$$

$$+ \Gamma \frac{|\chi_{H,F}|^2}{(\frac{\Gamma}{2})^2 + \Delta_{H,F}^2} \begin{pmatrix} H & 1 & F \\ m_h & q & m_f \end{pmatrix}^2 (\rho_{H,m_h} - \rho_{F,m_f}), \quad \textbf{(3a)}$$

$$\frac{d\rho_{F',m_{f'}}}{d\tau} = -\Gamma\rho_{F',m_{f'}} - \Gamma \sum_{G,m_g} \frac{|\chi_{F',G}|^2}{(\frac{\Gamma}{2})^2 + \Delta_{F',G}^2}$$

$$\times \begin{pmatrix} F' & 1 & G \\ m_{f'} & q & m_g \end{pmatrix}^2 (\rho_{F',m_{f'}} - \rho_{G,m_g}). \quad \textbf{(3b)}$$

These rate equations can be used to describe the time evolution of the population ρ in hyperfine ground states $|F, m_f\rangle$

[Eq. (3a)] and excited states $|F', m_{f'}\rangle$ [Eq. (3b)] [44–46], where F is the total angular momentum, and m_f is the magnetic projection quantum number. Here, Γ is the radiative rate, $\gamma_{G,H}$ is the population loading rate due to spontaneous emission for a specified ground state, $\chi_{G,H}$ is the effective Rabi frequency, $\Delta_{G,H}$ is the atom–field detuning, and the matrices $\begin{pmatrix} H & 1 & G \\ m_H & q & m_g \end{pmatrix}$ are the Clebsch–Gordon coefficients for transitions coupled by spin q. We note that this treatment ignores atomic coherences and the effects of collisions. Here, we treat the evolution of the $F = 3$ ground state populations in the presence of two optical pumping lasers resonant with the $F = 2 \rightarrow 3'$ and $F = 3 \rightarrow 3'$ transitions.

Figure 6 shows the simulated magnetic sublevel population distributions in the $F = 3$ ground state for (a) σ^+ and (b) linear (equal components σ^+ and σ^-) polarizations of optical pumping of duration τ. Here, we assume that the atoms are initially equally distributed in the magnetic sublevels of the $F = 3$ ground state.

In Fig. 6(a) we see that for σ^+ optical pumping, the population accumulates in the $m_f = +3$ sublevel, while the populations in the other sublevels show various transient forms of depletion. The same population dynamics occur for
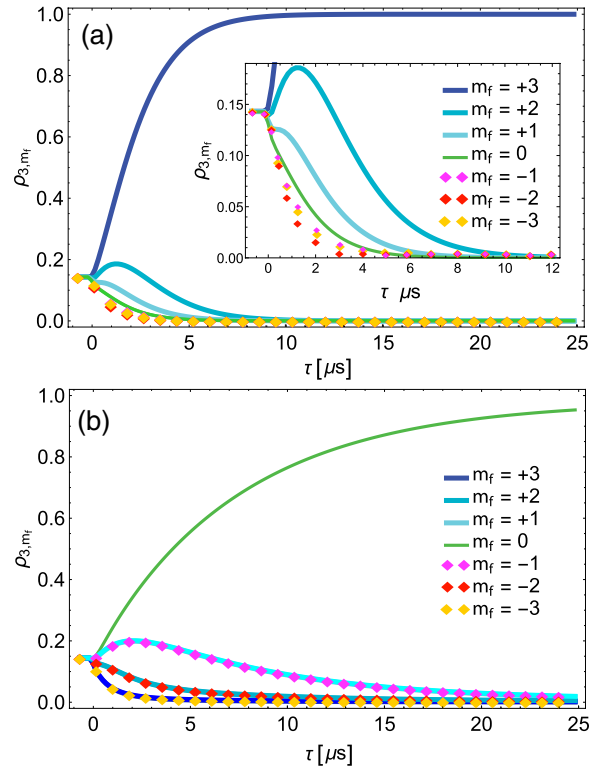

Fig. 6. Rate equation simulation of magnetic sublevel population distributions as a function of optical pumping time τ, for the $F = 3$ ground states based on Eqs. (3a) and (3b), for (a) σ^+ and (b) linear polarizations. Inset in (a) shows the transient decay of the $m_f = -3, -2, -1, 0, +1,$ and $+2$ states. Simulations assume a uniform population distribution at $t = 0$, a 50 µs resonant $F = 3 \rightarrow 3'$ optical pumping pulse with an intensity of 100 µW/cm², and a CW $F = 2 \rightarrow 3'$ repump beam with an intensity of 700 µW/cm².

the σ^- case (with accumulation of atoms in the $m_f = -3$ sublevel). These simulations are not shown. In contrast, for linearly polarized optical pumping, Fig. 6(b) shows the symmetric accumulation of the population in the $m_f = 0$ sublevel. This result is supported by the fluorescence spectra in Fig. 3(b) and corroborated by the data in Fig. 4(a).

Figure 7(a) shows the effective magnetic moment of the sample predicted by Eqs. (3a) and (3b) as a function of the optical pumping pulse duration τ. These predictions pertain to optical pumping with σ^+, σ^-, and linear polarizations. The vertical axis in this figure is expressed in units of $\langle\mu\rangle/(\mu_b g_f)$. Optical pumping to the stretched states, identifiable by the saturation of the effective magnetic moment at ± 3, occurs with a characteristic time constant of ~ 6 μs for our conditions. For linearly polarized optical pumping, the symmetric accumulation of atoms in the $F = 3$, $m_f = 0$ ground state defines the unchanging net magnetic moment.

Figure 7(b) shows simulated integrated vertical displacement as a function of τ for σ^+, σ^-, and linear optical pumping polarizations. For each polarization, the three curves represent the evolution of differing magnetic sublevel populations at $\tau = 0$,
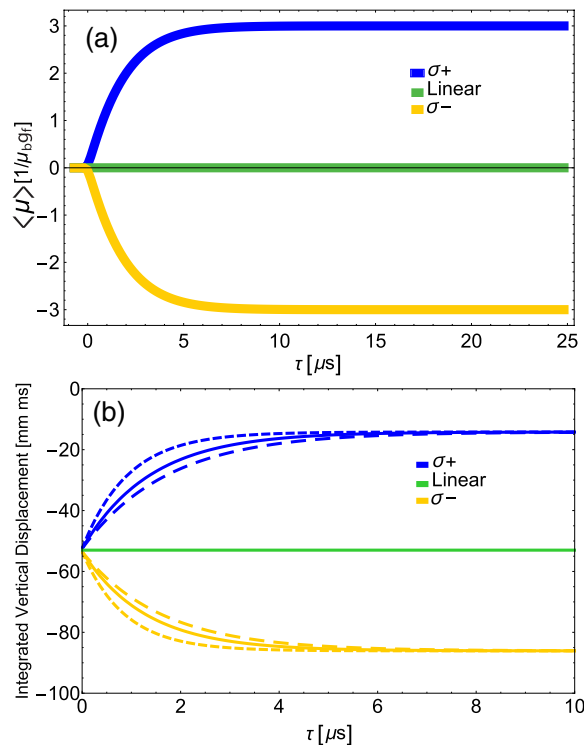

Fig. 7. (a) Simulated effective magnetic moment as a function of optical pumping time. Simulations assume a uniform population distribution at $t = 0$, a 50 μs resonant $F = 3 \rightarrow 3'$ optical pumping pulse with an intensity of 100 μW/cm², and a CW resonant $F = 2 \rightarrow 3'$ repump beam with an intensity of 700 μW/cm². (b) Simulated integrated vertical displacement as a function of optical pumping time, for a cloud in a vertical magnetic field gradient of 5 G/cm. For each optical pumping polarization, three curves represent different magnetic sublevel populations at $\tau = 0$: equal distribution (solid lines), exclusively in the $m_f = 0$ magnetic sublevel (short dashed lines), divided evenly in the $m_f = \pm 3$ sublevels (long dashed lines).

which shows the dependence of these predictions on initial conditions and demonstrates the sensitivity required to discriminate between these trajectories. Matching such curves to measured integrated displacements can allow the magnetic moment to be reconstructed and serve as a probe of the underlying magnetic sublevel population distribution.

C. Magnetic State Reconstruction and Possible Limitations

Figures 8(a) and 8(b) show, respectively, the integrated vertical and horizontal displacements calculated from trajectories of falling clouds observed for 40 ms, as functions of optical pumping pulse duration. These data points correspond to separate experiments, in which the samples have been optically pumped with σ^+, σ^-, and linear polarizations. The hashed areas specify the range of simulated values due to the experimental uncertainty of input parameters stated in Section 3. These curves are generated by assuming equally populated ground states at $\tau = 0$, and numerically integrating simulated trajectories, described by Eqs. (1a) and (1b), over drop intervals of 40 ms. The measurements show that this technique can unambiguously discriminate between population distributions that have been progressively pumped to extreme states. The excellent agreement between the data and the simulations shows the effectiveness of our technique to measure net magnetic moments by photographing falling clouds. Additionally, the agreement over the range of optical pumping times serves to verify the dynamic evolution of the magnetic sublevel populations predicted by Eqs. (3a) and (3b) for a specified initial population distribution. This agreement also suggests that it may be possible to reconstruct the magnetic sublevel population distribution for all τ. Nevertheless, the spread in trajectory evolution due to the uncertainties imposed by experimental parameters and the similarity in the integrated displacement curves for different initial conditions [see Fig. 7(b)] indicate that our technique has limitations for measuring magnetic sublevel populations.

Despite these limitations, it is possible to envision how this technique could be used to extract information from a sample with an unknown initial population distribution. The protocol for such a measurement would involve determining the integrated displacements resulting from all three polarizations of optical pumping, and the use of iterative trajectory simulations to match the data so as to identify the starting distribution as illustrated in Fig. 7(b). However, detailed comparison with a complementary technique, such as RF absorption spectroscopy, would be required to understand the suitability of this approach.

D. Trajectory Analysis

We hypothesize that our model, which assumes adiabatic evolution of magnetic moments, is successful in recreating the optical pumping results because $B_{\text{tot}} = \sqrt{B_x^2 + B_y^2 + B_z^2}$ sampled by the centroid of the cloud is suitably offset from zero across the entire observation window.

While a number of theoretical models for Majorana transitions can be used to support the observed trends [47–49], we find that a straightforward characterization can be based on the adiabaticity parameter $\alpha = \omega_L/(\partial\theta/\partial t)$, where ω_L is the local
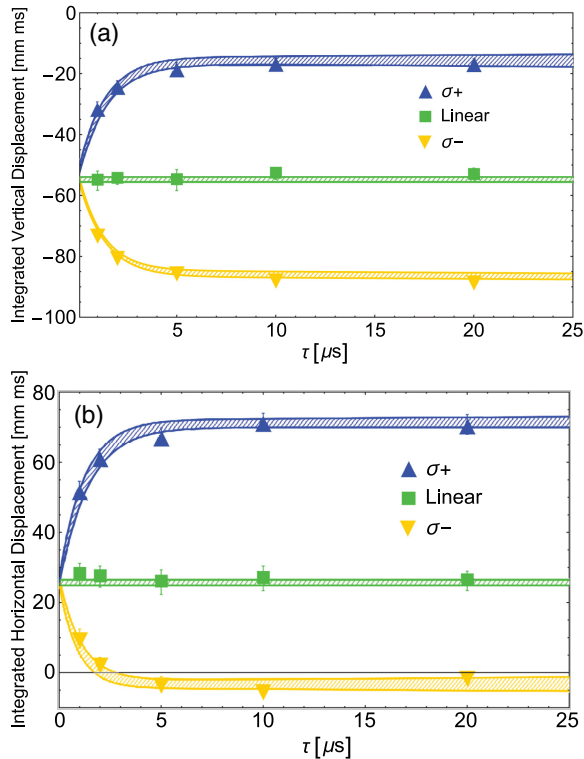
Fig. 8. Integrated displacement of a cloud falling in a 5 G/cm vertical magnetic field gradient as a function of optical pumping time for (a) vertical and (b) horizontal directions. The hashed areas show the range of simulated integrated displacements (within experimental uncertainty of the input parameters) for three polarizations of optical pumping beam: $\sigma+$ blue (dark gray), linear green (gray), and $\sigma-$ orange (light gray).

Larmor frequency and θ is the azimuthal angle of the magnetic field [50]. For our conditions, we find that $\alpha \gg 1$ throughout the observation window, suggesting that the probability for non-adiabatic transitions is correspondingly small. Although we have not considered magnetic field variations over the entire cloud, this conjecture is supported by the finding that trajectory simulations assuming fully non-adiabatic evolution of magnetic moments do not match experimental data as well as simulations that assume adiabatic evolution. In these simulations, adiabatic evolution refers to trajectories governed by Eqs. (1a) and (1b), where $\langle \mu(t) \rangle$ is aligned with the local magnetic field for each time step in the simulation. In contrast, for simulations of non-adiabatic evolution, $\langle \mu(t) \rangle$ is anti-aligned with the local field after passing through a magnetic field zero.

5. CONCLUSION

We have presented a simple technique to characterize the magnetic moments in a typical MOT, with $T \approx 100 \, \mu K$, for which the local magnetic fields are well known. This work also explores the sensitivity of the technique to reconstruct the underlying magnetic sublevel population distributions. A defining aspect of this technique is that it does not rely on the spatial separation of magnetic sublevels, as in previous Stern–Gerlach experiments

involving MOTs, atomic beams, and BECs. As such, this technique is readily applicable in situations where experimental constraints preclude the use of long drop zones, large magnetic field gradients, or ultra-cold temperatures necessary to observe spatial separation of the magnetic sublevels. A disadvantage of this technique (in comparison with absorption spectroscopy) is the limited sensitivity to variations in the initial distributions. However, this technique involves a much simpler setup than absorption or fluorescence spectroscopy experiments in which spectra are recorded by sweeping or amplitude modulating a probe laser after the application of a magnetic field gradient to Zeeman shift the sublevels. Both the advantages and disadvantages can be better understood through a direct comparison with other methods such as absorption spectroscopy [16,22–25]. We expect that our technique may be suitable for the rapid characterization of portable sources of cold atoms that are optically pumped with well specified optical or RF sources. A more detailed analysis that considers the magnetic field variations across the spatial extent of the cloud can be expected to produce even better quantitative agreement with the observed trends. Additionally, although we have verified that the cloud does not move appreciably along the third direction (y), it is also possible that simultaneously tracking the cloud along y using a second CCD camera would provide redundancy and refine the modeling.

Disclosures. The authors declare no conflicts of interest.

REFERENCES

1. E. L. Raab, M. Prentiss, A. Cable, S. Chu, and D. E. Pritchard, "Trapping of neutral sodium atoms with radiation pressure," Phys. Rev. Lett. **59**, 2631–2634 (1987).

2. C. Monroe, W. Swann, H. Robinson, and C. Wieman, "Very cold trapped atoms in a vapor cell," Phys. Rev. Lett. **65**, 1571–1574 (1990).

3. J. L. Roberts, N. R. Claussen, S. L. Cornish, and C. E. Wieman, "Magnetic field dependence of ultracold inelastic collisions near a Feshbach resonance," Phys. Rev. Lett. **85**, 728–731 (2000).

4. M. H. Anderson, J. R. Ensher, M. R. Matthews, C. E. Wieman, and E. A. Cornell, "Observation of Bose-Einstein condensation in a dilute atomic vapor," Science **269**, 198–201 (1995).

5. K. B. Davis, M.-O. Mewes, M. R. Andrews, N. J. van Druten, D. S. Durfee, D. M. Kurn, and W. Ketterle, "Bose-Einstein condensation in a gas of sodium atoms," Phys. Rev. Lett. **75**, 3969–3973 (1995).

6. M. Greiner, O. Mandel, T. Esslinger, T. W. Hänsch, and I. Bloch, "Quantum phase transition from a superfluid to a Mott insulator in a gas of ultracold atoms," Nature **415**, 39–44 (2002).

7. C. Fertig and K. Gibble, "Measurement and cancellation of the cold collision frequency shift in an 87 Rb fountain clock," Phys. Rev. Lett. **85**, 1622–1625 (2000).

8. K. Gibble and S. Chu, "Laser-cooled Cs frequency standard and a measurement of the frequency shift due to ultracold collisions," Phys. Rev. Lett. **70**, 1771–1774 (1993).

9. A. Peters, K. Y. Chung, and S. Chu, "Measurement of gravitational acceleration by dropping atoms," Nature **400**, 849–852 (1999).

10. M. Kasevich and S. Chu, "Atomic interferometry using stimulated Raman transitions," Phys. Rev. Lett. **67**, 181–184 (1991).

11. R. H. Parker, C. Yu, W. Zhong, B. Estey, and H. Müller, "Measurement of the fine-structure constant as a test of the standard model," Science **360**, 191–195 (2018).

12. B. Barrett, P.-A. Gominet, E. Cantin, L. Antoni-Micollier, A. Bertoldi, B. Battelier, P. Bouyer, J. Lautier, and A. Landragin, "Mobile and remote inertial sensing with atom interferometers," in *Atom Interferometry*, Proceedings of the International School of Physics "Enrico Fermi" (2014), Vol. **188**, pp. 493–555.

13. E. R. Elliott, M. C. Krutzik, J. R. Williams, R. J. Thompson, and D. C. Aveline, "NASA's cold atom lab (CAL): system development and ground test status," npj Microgravity **4**, 16 (2018).

14. H. Müntinga, H. Ahlers, M. Krutzik, A. Wenzlawski, S. Arnold, D. Becker, K. Bongs, H. Dittus, H. Duncker, N. Gaaloul, C. Gherasim, E. Giese, C. Grzeschik, T. Haensch, O. Udo Hellmig, W. Herr, S. Herrmann, E. Kajari, S. Kleinert, C. Lämmerzahl, W. Lewoczko-Adamczyk, J. I. Malcolm, N. Meyer, R. Nolte, A. Peters, M. Popp, J. Reichel, A. Roura, J. Rudolph, M. Schiemangk, M. Schneider, S. T. Seidel, T. Valenzuela, A. Vogel, R. Walser, T. Wendrich, P. Windpassinger, W. Zeller, T. van Zoest, W. Ertmer, W. P. Schleich, and E. M. Rasel, "Interferometry with Bose-Einstein condensates in microgravity," Phys. Rev. Lett. **110**, 093602 (2013).

15. D. Becker, M. D. Lachmann, S. T. Seidel, H. Ahlers, A. N. Dinkelaker, J. Grosse, O. Hellmig, H. Müntinga, V. Schkolnik, T. Wendrich, A. Wenzlawski, B. Weps, R. Corgier, T. Franz, N. Gaaloul, W. Herr, D. Lüdtke, M. Popp, S. Amri, H. Duncker, M. Erbe, A. Kohfeldt, C. Braxmaier, E. Charron, W. Ertmer, M. Krutzik, C. Lämmerzahl, A. Peters, W. P. Schleich, K. Sengstock, R. Walser, A. Wicht, P. Windpassinger, and E. M. Rasel, "Space-borne Bose–Einstein condensation for precision interferometry," Nature **562**, 391 (2018).

16. K. E. Gibble, S. Kasapi, and S. Chu, "Improved magneto-optic trapping in a vapor cell," Opt. Lett. **17**, 526–528 (1992).

17. Y.-C. Chen, Y.-A. Liao, L. Hsu, and I. A. Yu, "Simple technique for directly and accurately measuring the number of atoms in a magneto-optical trap," Phys. Rev. A **64**, 031401 (2001).

18. M. L. Terraciano, M. Bashkansky, and F. K. Fatemi, "A single-shot imaging magnetometer using cold atoms," Opt. Express **16**, 13062–13069 (2008).

19. M. L. Terraciano, M. Bashkansky, and F. K. Fatemi, "Faraday spectroscopy of atoms confined in a dark optical trap," Phys. Rev. A **77**, 063417 (2008).

20. K. Sycz, A. M. Wojciechowski, and W. Gawlik, "Atomic-state diagnostics and optimization in cold-atom experiments," Sci. Rep. **8**, 1 (2018).

21. P. D. Kunz, D. H. Meyer, and F. K. Fatemi, "Twists in nonlinear magneto-optic rotation with cold atoms," Opt. Express **25**, 16392–16399 (2017).

22. S. Cauchi, A. Vorozcovs, M. Weel, S. Beattie, O. Gagnon, and A. Kumarakrishnan, "Absorption spectroscopy of trapped rubidium atoms," Can. J. Phys. **82**, 905–916 (2004).

23. A. Vorozcovs, M. Weel, S. Beattie, S. Cauchi, and A. Kumarakrishnan, "Measurements of temperature scaling laws in an optically dense magneto-optical trap," J. Opt. Soc. Am. B **22**, 943–950 (2005).

24. M. A. Kasevich, E. Riis, S. Chu, and R. G. DeVoe, "Rf spectroscopy in an atomic fountain," Phys. Rev. Lett. **63**, 612–615 (1989).

25. C. W. White, W. M. Hughes, G. S. Hayne, and H. G. Robinson, "Determination of g-factor ratios for free Rb^{85} and Rb^{87} atoms," Phys. Rev. **174**, 23–32 (1968).

26. L. S. Goldner, C. Gerz, R. J. C. Spreeuw, S. L. Rolston, C. I. Westbrook, W. D. Phillips, P. Marte, and P. Zoller, "Momentum transfer in laser-cooled cesium by adiabatic passage in a light field," Phys. Rev. Lett. **72**, 997–1000 (1994).

27. É. Maréchal, S. Guibal, J.-L. Bossennec, M.-P. Gorza, R. Barbé, J.-C. Keller, and O. Gorceix, "Longitudinal Stern-Gerlach effect for slow cesium atoms," Eur. Phys. J. D **2**, 195–198 (1998).

28. W. Gerlach and O. Stern, "Der experimentelle nachweis des magnetischen momentes des silberatoms," Z. Phys. A **8**, 110–111 (1922).

29. W. Gerlach and O. Stern, "Der experimentelle nachweis der richtungsquantelung im magnetfeld," Z. Phys. A **9**, 349–352 (1922).

30. F. Lison, P. Schuh, D. Haubrich, and D. Meschede, "High-brilliance Zeeman-slowed cesium atomic beam," Phys. Rev. A **61**, 013405 (1999).

31. C. Käfer, R. Bourouis, J. Eurisch, A. Tripathi, and H. Helm, "Ejection of magnetic-field-sensitive atoms from an optical dipole trap," Phys. Rev. A **80**, 023409 (2009).

32. D. M. Stamper-Kurn, M. R. Andrews, A. P. Chikkatur, S. Inouye, H.-J. Miesner, J. Stenger, and W. Ketterle, "Optical confinement of a Bose-Einstein condensate," Phys. Rev. Lett. **80**, 2027–2030 (1998).

33. S. Dürr, T. Volz, A. Marte, and G. Rempe, "Observation of molecules produced from a Bose-Einstein condensate," Phys. Rev. Lett. **92**, 020406 (2004).

34. E. M. Bookjans, A. Vinit, and C. Raman, "Quantum phase transition in an antiferromagnetic spinor Bose-Einstein condensate," Phys. Rev. Lett. **107**, 195306 (2011).

35. Y.-J. Lin, K. Jiménez-Garca, and I. B. Spielman, "Spin–orbit-coupled Bose–Einstein condensates," Nature **471**, 83–86 (2011).

36. J. Y. Choi, W. J. Kwon, and Y. I. Shin, "Observation of topologically stable 2D Skyrmions in an antiferromagnetic spinor Bose-Einstein condensate," Phys. Rev. Lett. **108**, 035301 (2012).

37. G. Carlse, A. Pouliot, T. Vacheresse, A. Carew, H. Beica, and A. Kumarakrishnan, "Technique for in-situ measurement of magnetic sublevel populations in a magneto-optical trap based on free-expansion imaging," in *Conference on Coherence and Quantum Optics* (Optical Society of America, 2019), paper W6A-10.

38. D. Guéry-Odelin, J. Söding, P. Desbiolles, and J. Dalibard, "Strong evaporative cooling of a trapped cesium gas," Opt. Express **2**, 323–329 (1998).

39. H. C. Beica, A. Pouliot, A. Carew, A. Vorozcovs, N. Afkhami-Jeddi, G. Carlse, P. Dowling, B. Barron, and A. Kumarakrishnan, "Characterization and applications of auto-locked vacuum-sealed diode lasers for precision metrology," Rev. Sci. Instrum. **90**, 085113 (2019).

40. B. Barrett, A. Carew, H. Beica, A. Vorozcovs, A. Pouliot, and A. Kumarakrishnan, "Prospects for precise measurements with echo atom interferometry," Atoms **4**, 19 (2016).

41. B. Barrett, I. Chan, and A. Kumarakrishnan, "Atom-interferometric techniques for measuring uniform magnetic field gradients and gravitational acceleration," Phys. Rev. A **84**, 063623 (2011).

42. B. Barrett, A. Carew, S. Beattie, and A. Kumarakrishnan, "Measuring the atomic recoil frequency using a modified grating-echo atom interferometer," Phys. Rev. A **87**, 033626 (2013).

43. I. Chan, B. Barrett, and A. Kumarakrishnan, "Precise determination of atomic g-factor ratios from a dual isotope magneto-optical trap," Phys. Rev. A **84**, 032509 (2011).

44. A. Pouliot, H. C. Beica, A. Carew, A. Vorozcovs, G. Carlse, B. Barrett, and A. Kumarakrishnan, "Investigations of optical pumping for magnetometry using an auto-locking laser system," Proc. SPIE **10637**, 106370A (2018).

45. B. Barrett, "Techniques for measuring the atomic recoil frequency using a grating-echo atom interferometer," Ph.D. thesis (York University, 2012).

46. P. R. Berman, G. Rogers, and B. Dubetsky, "Rate equations between electronic-state manifolds," Phys. Rev. A. **48**, 1506–1513 (1993).

47. K. B. Davis, "Evaporative cooling of sodium atoms," Ph.D. thesis (Massachusetts Institute of Technology, 1995).

48. J. R. Rubbmark, M. M. Kash, M. G. Littman, and D. Kleppner, "Dynamical effects at avoided level crossings: a study of the Landau-Zener effect using Rydberg atoms," Phys. Rev. A. **23**, 3107–3117 (1981).

49. C. V. Sukumar and D. M. Brink, "Spin-flip transitions in a magnetic trap," Phys. Rev. A **56**, 2451–2454 (1997).

50. R. Hight, R. Robiscoe, and W. Thorson, "Nonadiabatic spin transitions in an inhomogeneous magnetic field," Phys. Rev. A. **15**, 1079–1087 (1977).